Energy & Environmental Science

PAPER

View Article Online
View Journal

Cite this: DOI: 10.1039/c9ee01493d

Detailed-balance analysis of Yb^{3+}:$CsPb(Cl_{1-x}Br_x)_3$ quantum-cutting layers for high-efficiency photovoltaics under real-world conditions†

Matthew J. Crane, Daniel M. Kroupa and Daniel R. Gamelin *

Yb^{3+}-Doped lead-halide perovskites (Yb^{3+}:$CsPb(Cl_{1-x}Br_x)_3$) have emerged as unique materials combining strong, tunable broadband absorption with near-infrared photoluminescence quantum yields (PLQYs) approaching 200% at ambient temperature. These remarkable properties make Yb^{3+}:$CsPb(Cl_{1-x}Br_x)_3$ an extremely promising candidate for spectral shaping in high-efficiency photovoltaic devices. Previous theoretical assessments of such "downconversion" devices have predicted single-junction efficiencies up to 40%, but have been highly idealized. Real materials like Yb^{3+}:$CsPb(Cl_{1-x}Br_x)_3$ have practical limitations such as constrained band-gap and PL energies, non-directional emission, and an excitation-power-dependent PLQY. Hence, it is unclear whether Yb^{3+}:$CsPb(Cl_{1-x}Br_x)_3$, or any other non-ideal quantum-cutting material, can indeed boost the efficiencies of real high-performance PV. Here, we examine the thermodynamic, detailed-balance efficiency limit of Yb^{3+}:$CsPb(Cl_{1-x}Br_x)_3$ on different existing PV under real-world conditions. Among these, we identify silicon heterojunction technology as very promising for achieving significant performance gains when paired with Yb^{3+}:$CsPb(Cl_{1-x}Br_x)_3$, and we predict power-conversion efficiencies of up to 32% for this combination. Surprisingly, PL saturation does not negate the improved device performance. Calculations accounting for actual hourly incident solar photon fluxes show that Yb^{3+}:$CsPb(Cl_{1-x}Br_x)_3$ boosts power-conversion efficiencies at all times of day and year in two representative geographic locations. Predicted annual energy yields are comparable to those of tandem perovskite-on-silicon technologies, but without the need for current matching, tracking, or additional electrodes and inverters. In addition, we show that band-gap optimization in real quantum cutters is inherently a function of their PLQY and the ability to capture that PL. These results provide key design rules needed for development of high-efficiency quantum-cutting photovoltaic devices based on Yb^{3+}:$CsPb(Cl_{1-x}Br_x)_3$.

Received 9th March 2019,
Accepted 30th May 2019

DOI: 10.1039/c9ee01493d

rsc.li/ees

Broader context

The roadmap to global adoption of solar technology requires the development of highly efficient, low-cost photovoltaic (PV) devices with power-conversion efficiencies (PCEs) approaching or exceeding 30%. Rather than developing entirely new technology platforms, an attractive route to achieving this goal is to build on existing, successful PV technologies like silicon, thereby reducing risk and capital expenditure. The excitement around metal-halide perovskites, with their highly tunable characteristics and high PV performance, stems in part from their potential to fulfill this role by pairing with silicon in tandem PV architectures. A new alternative to tandem PVs has recently emerged, however; doped perovskites, with photoluminescence quantum efficiencies approaching 200% achieved *via* quantum cutting, offer untapped potential for PV enhancement by spectral downconversion, without the technical drawbacks of true tandem devices. Although promising, virtually nothing is yet known about the solar performance of these unique quantum-cutting downconverters under real-world conditions, or what their optimized characteristics should be for pairing with existing and upcoming PV technologies. This study uses real-world solar irradiance, PV, and perovskite quantum-cutting data to model and assess the performance of these quantum cutters as solar spectral downconverters on PV cells. We demonstrate that application of a perovskite quantum-cutting layer onto existing PV cells can yield PCEs over 30% and relative increases in annual power generation of over 20%. This study validates the attractiveness of these unique broadband quantum-cutting materials and outlines both general and specific pathways for their application in high-performance PV technologies.

Introduction

A major limitation of conventional single-junction photovoltaics (PVs) is their inefficient conversion of high-energy solar photons into electricity.[1] The excess energy that blue and ultraviolet (UV) photons possess beyond what is needed to span the absorber's band gap is lost as heat rather than captured as useable power. These thermalization losses constitute nearly half of all energy-conversion losses at the Shockley–Queisser, thermodynamic efficiency maximum, limiting theoretical single-junction power-conversion efficiencies (PCEs) to only 33%.[2,3] One popular strategy

Department of Chemistry, University of Washington, Seattle, WA 98195-1700, USA. E-mail: gamelin@chem.washington.edu

† Electronic supplementary information (ESI) available. See DOI: 10.1039/c9ee01493d

for overcoming such thermalization losses is to construct "tandem" or multi-junction PVs, in which two or more current-matched junctions are stacked in optical and electrical series, each collecting a different fraction of the solar spectrum.[4–7] In a standard two-terminal tandem PV, the device operates at a single rate-limiting photocurrent, and the voltages from the two junctions are summed. Although tandem and multi-junction PVs offer high theoretical solar PCEs (~46% for a two-terminal tandem PV[8]), their large-scale implementation is challenging because they generally require expensive solar-tracking installations to ensure optimal current matching across the two junctions, and they often also require expensive, substrate- and materials-compatible fabrication steps[9] to ensure high-quality contacts and serial interfaces,[10] increasing the cost per watt.[11] Four-terminal PV devices avoid current-matching limitations but require additional hardware including inverters, wiring, soldering, *etc.*, increasing the balance-of-systems costs.[12–14]

An alternative strategy for eliminating thermalization losses involves modifying single-junction PVs with quantum-cutting (QC) spectral-downconversion layers that convert blue/UV photons into lower-energy photons with photoluminescence quantum yields (PLQYs) exceeding 100%. In such a device, the down-conversion layer is only in optical series with the PV, eliminating the need for wiring, current matching, and defect-free interfacing. Using idealized quantum cutters with optimized broadband visible absorption, narrow-band near-infrared (near-IR) PL, and PLQYs of 200%, detailed-balance calculations have projected that quantum cutting can increase maximum thermodynamic single-junction PV PCEs from 31% for a single-junction Si PV[15] up to 40%[3] for the same Si PV with an idealized QC layer. QC downconversion thus has the potential to substantially enhance efficiencies of conventional PV technologies with minimal additional module manufacturing or installation costs.

Unfortunately, until recently there has not been an experimentally demonstrated material that exhibits the desired combination of tunable broadband absorption with a high absorption cross section, narrow-band near-IR PL, and 200% PLQY to realize these potential benefits. Quantum cutting is indeed a well-established photophysical phenomenon in the research laboratory,[16–18] but it has generally been demonstrated using combinations of lanthanide ions for both absorption and emission steps of the process. In some cases, lanthanide-based QC materials have shown very high PLQYs of ~180%, but the small absorption cross-sections of the lanthanide f–f transitions limit their solar utility. Efforts to integrate strongly absorbing broadband sensitizers with QC materials have demonstrated fundamental advances but have not yet succeeded in generating the requisite broad solar absorption while retaining high PLQYs.[1,17,19] PV applications of quantum cutters have thus never proven practical.

Recently, colloidal Yb^{3+}-doped $CsPb(Cl_{1-x}Br_x)_3$ perovskite nanocrystals (NCs) were demonstrated to show broadband sensitization of Yb^{3+} near-IR PL (1.26 eV) with very large absorption cross-sections and experimental PLQYs as high as ~200%.[20–22] Spectroscopic studies have revealed a unique picosecond QC mechanism and QC energy efficiencies of nearly unity.[20,23] NC deposition onto the front surfaces of commercial crystalline Si PV has been reported to yield a remarkable 3.4% absolute PCE gain (18.1 → 21.5%) under one-sun illumination,[24] providing a compelling proof of concept for PV applications of these materials. Further work demonstrated that Yb^{3+}:$CsPb(Cl_{1-x}Br_x)_3$ polycrystalline thin films exhibit identical QC characteristics,[21] revealing that this QC is a bulk phenomenon and opening the door to various industrially relevant thin-film deposition methodologies for commercial device fabrication.[25,26]

Although extremely promising, there are still several outstanding fundamental questions about the properties and potential limitations of this QC material that will ultimately determine its commercial viability as a solar spectral downconverter and a competitor with tandem PV. For example, one potential limitation is the occurrence of PL saturation with modest excitation fluences, including those experienced under one-sun illumination.[27] A second potential limitation relates to whether it will be necessary to capture all of the photons emitted from the QC layer with the underlying PV, or whether some non-ideality would still yield overall device gains.[28–31] Less obvious are questions pertaining to how the real-world physical characteristics of these materials (*e.g.*, band-gap energy, PLQY, *etc.*) might influence device design and performance. Whereas previous detailed-balance calculations idealized these important physical characteristics to identify theoretical performance limits for QC/PV devices, these factors are constrained in real materials.[32] Given that Yb^{3+}:$CsPb(Cl_{1-x}Br_x)_3$ is the first material that has been experimentally demonstrated to simultaneously possess tunable, strong, and broadband absorption, narrow near-IR PL, and PLQYs of essentially 200%, it is now of timely interest to assess the real-world PCE limits of QC/PV devices based on this material.[33]

Here, we perform detailed modeling and analysis of device characteristics that can be expected from integration of Yb^{3+}:$CsPb(Cl_{1-x}Br_x)_3$ quantum cutters with a single-junction PV. We consider the effects of $CsPb(Cl_{1-x}Br_x)_3$ band gap energy and PLQY, the external quantum efficiency (EQE) of the PV itself, the PL capture efficiency, seasonal and daily variations in solar irradiance, and QC PL saturation effects, all based on experimental input data. Our analysis allows several important conclusions. First, we demonstrate a relationship between the QC band-gap energy and the overall QC efficiency (PLQY and capture) that will steer the design of actual rather than idealized devices. We assess the impact of PL saturation on device performance in two geographic locations and demonstrate that significant gains are anticipated even without taking any steps to remediate this saturation or to improve capture. As the first modeling and analysis of QC/PV devices based on Yb^{3+}:$CsPb(Cl_{1-x}Br_x)_3$ quantum cutters, these results are anticipated to provide valuable guidance for future development and optimization of this technology.

Methods

For detailed-balance calculations, we consider the geometry presented in Fig. 1A, involving a QC layer stacked on top of a PV with a perfect reflective electrode.[3] The PCE of the QC/PV device is defined as the ratio of power produced by the device, P_{device}, to the power incident on the device, P_{sun},

$$\mathrm{PCE} = \frac{P_{\mathrm{device}}}{P_{\mathrm{sun}}} = \frac{J_{\mathrm{op}} V_{\mathrm{op}}}{\int_0^\infty \Phi_{\mathrm{AM1.5G}} \mathrm{d}\lambda} \quad (1)$$

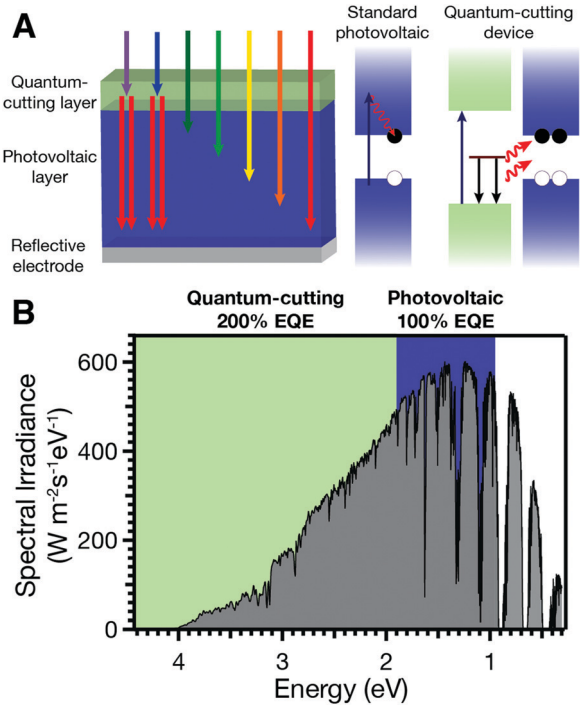

Fig. 1 (A) Schematic of the proposed QC/PV architecture and QC mechanism. In the ideal QC/PV device, the high-band gap QC layer downconverts absorbed sunlight, emitting photons at one half its band gap with 200% QY. The PV device absorbs all of the downconverted, emitted photons and generates photocurrent with 100% EQE, doubling the photocurrent from the high-energy region of the AM1.5G spectrum. Solar photons with energies below the QC band gap are transmitted directly to the PV layer, where they also produce photocurrent with 100% EQE if above the PV energy gap. (B) The optimum regions of absorption for the QC (green) and PV (blue) layers in an idealized QC/PV device. In real QC/PV devices, both the QC and PV layers operate with quantum efficiencies below 200% and 100%, respectively.

Here, $\Phi_{AM1.5G}$ (one sun) is the solar spectral irradiance, taken from the American Society for Testing and Materials G-173 with units of W m^{-2} eV^{-1}, J_{op} is the operating current per unit area, and V_{op} is the operating voltage. In this model, we employ the detailed balance first proposed by Shockley and Queisser wherein the PV cell operates as a blackbody emitter without non-radiative recombination or defects.[15] Briefly, the PV's photocurrent is determined by the rate at which it absorbs incident photons from both the QC layer and the transmitted AM1.5G spectrum less the bias-dependent radiative emission rate,

$$J = J_{sc} - J_0 \tag{2}$$

The cell's emission rate is modeled as a generalization of the Stefan–Boltzmann Law using Kirchoff's Law as

$$J_0 = \frac{2\pi n^2}{h^3c^2}\int_0^\infty \frac{q(q\Phi_{AM1.5G})^2\alpha_{PV}}{\exp\left(\frac{E-qV}{kT}\right)-1}\mathrm{d}E \tag{3}$$

where α_{PV}, n, and T are the absorption probability, refractive index, and temperature of the PV layer, and h, c, q, and k are Planck's constant, the speed of light, the elementary charge of an electron, and Boltzmann's constant, respectively.[2] We assume an ideal reflective electrode such that the PV cell only emits from the half cone of its front surface.

The contribution of the quantum cutter and the incident solar flux to the photocurrent is

$$J_{sc} = q\int_0^\infty (\alpha_{PV} - \alpha_{QC})\Phi_{AM1.5G} + \bar{\alpha}_{PV}(E_{QC})\phi\xi\alpha_{QC}\Phi_{AM1.5G}\mathrm{d}E \tag{4}$$

where α_{QC} is the absorption probability of the quantum cutter, ξ is the efficiency of optical coupling between the QC and PV layers, ϕ is the PLQY of the QC material, and $\bar{\alpha}_{PV}(E_{QC})$ is the absorption probability of the PV material, weighted by spectral bandwidth and energy of the quantum cutter's PL, $\bar{\alpha}_{PV}(E_{QC}) = \int_0^\infty \alpha_{PV}(E)I_{QC}(E)\mathrm{d}E / \int_0^\infty I_{QC}(E)\mathrm{d}E$. Here, $I_{QC}(E)$ is the spectral line shape of the quantum cutter's PL. For perfect PV devices, the PV cell's efficiency of absorption and conversion to photocurrent—that is, its EQE—is a step function with the PV absorbing all light above its band gap and converting this to photocurrent. When modeling real-world devices, the absorption of the device is defined by experimentally measured EQE data, which include the effects of non-radiative recombination, reflections, and parasitic absorption. In these ideal limits, the operating voltage and operating current are found by solving the equation,

$$\frac{\mathrm{d}JV}{\mathrm{d}V} = 0 \tag{5}$$

As analyzed extensively by De Vos *et al.*,[28] there are many possible schemes to enhance optical coupling from a spectral downconversion layer into a PV cell, including optimizing refractive index values, antireflective coatings, or Bragg reflectors, *etc.* Similarly, while most analyses assume that the QC layer downconverts with 200% PLQY and exhibits narrowband photoluminescence at precisely half of its band-gap energy, practical devices will never exhibit these properties. To describe all possible device options, we define an overall quantum-cutting efficiency, η, as

$$\eta = \xi \times \phi \tag{6}$$

Similarly, for these calculations, the refractive index of the QC layer matches the index of the PV device to avoid geometry-dependent refractive-index effects. By the same virtue, these calculations do not include the potential benefits of adding an additional optical layer, such as a graded antireflective coating, passivation layer, or reduced heating. Table S1 (ESI†) lays out the symbols used in the text and their meaning.

Results and discussion

Fig. 1A compares the operation of a standard PV device with a QC/PV device. In a standard PV device, absorption of a high-energy photon produces a hot electron and hole, which rapidly thermalize to the conduction- and valence-band edges prior to carrier extraction and power generation. For an optimized, standard PV device, these thermalization losses comprise ~33% of the incident energy from the sun.[2] Fig. 1A also shows a schematic of the QC/PV device architecture that we consider

in this manuscript. In this device, the QC layer absorbs high-energy photons and transmits low-energy photons. The QC layer downconverts and emits the energy from absorbed high-energy photons with a PLQY that exceeds 100% stemming from a mechanism known as quantum cutting.[34] Subsequent absorption of this downconverted light by the PV layer improves the overall PCE by converting the voltage typically lost to thermalization in a standard PV device into extra photocurrent in the QC/PV device. A perfect QC layer absorbs at twice the band gap of the PV layer and emits precisely at the band gap of the PV layer to minimize thermalization losses and thus maximize the QC energy efficiency. In the limit of perfect operation, the device design balances increases in photocurrent from maximizing QC layer absorption (and hence decreasing the PV band gap) against increases in the device operating voltage (from increasing the PV bandgap).

Fig. 1B illustrates ideal use of the AM1.5G spectrum by a perfect QC/PV device. In practice, of course, the PLQY of the QC layer is $<200\%$, the EQE of the PV device at the energy of the QC photoluminescence is $<100\%$, and isotropic emission of the QC layer limits capture of downshifted emission by the PV layer.[30,31] Because these factors can vary significantly with material composition and device geometry, we employ η as the figure of merit for QC/PV device analysis.

Fig. 2A plots the maximum operating PCE of a QC/PV device as a function of both the PV band gap and η, assuming perfect Shockley–Queisser behavior of the PV layer.[35] At large PV band gaps, the AM1.5G spectrum contains insufficient ultraviolet photons for the QC layer to improve the photocurrent, and the device performance is independent of η. Conversely, at low PV band gaps, the QC layer itself experiences greater thermalization losses, the PV voltage decreases, and the device performance suffers. At intermediate values, addition of a QC layer with any η greater than 100% improves the device PCE by boosting the photocurrent.

Fig. 2B shows slices from the plot in Fig. 2A, highlighting the PCE at different values of η. The black dots illustrate the ideal PV band gap, which shifts with η. For a given incident solar spectrum, there exists an optimum PV band-gap that maximizes both photocurrent and photovoltage. Changing η reshapes the incident solar spectrum, and the optimum PV band gap shifts.[1,36] Fig. 2C presents the ideal QC band gap for different η. Surprisingly, the ideal QC band gap can vary from 1.90 to 2.67 eV. The discrete jumps in the optimum band gap reflect the AM1.5G spectra and the step-function responses of idealized QC and PV materials. These results provide valuable general design rules for the development of future QC/PV devices.

We now turn to analysis of specific real-world scenarios based on integration of existing QC and PV components to develop optimized QC/PV devices, focusing on Yb^{3+}:$CsPb(Cl_{1-x}Br_x)_3$ as the QC layer. Fig. 3A illustrates the tunable absorption of Yb^{3+}:$CsPb(Cl_{1-x}Br_x)_3$ achievable through anion alloying, and the Yb^{3+} $^2F_{5/2} \rightarrow {}^2F_{7/2}$ photoluminescence that results from above-band-gap Yb^{3+}:$CsPb(Cl_{1-x}Br_x)_3$ photoexcitation.[20,21] Unlike the idealized QC model, the Yb^{3+}:$CsPb(Cl_{1-x}Br_x)_3$ photoluminescence does not shift with the $CsPb(Cl_{1-x}Br_x)_3$ band gap, and instead remains fixed at a constant energy of $\sim$1.26 eV.

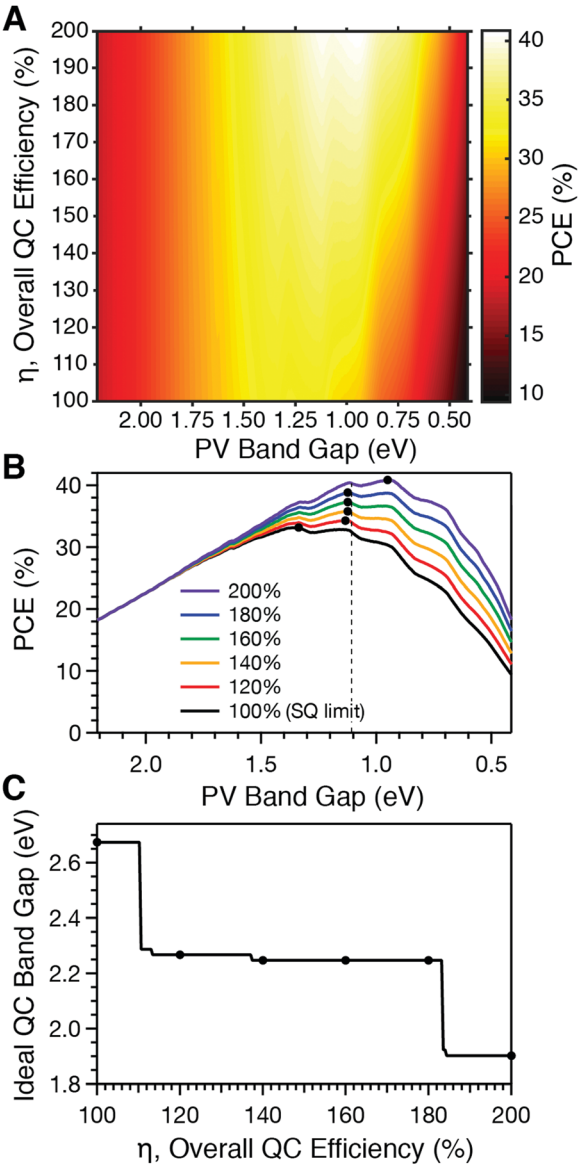

Fig. 2 (A) The detailed-balance maximum PCEs of a non-ideal QC layer on a Shockley–Queisser PV cell. In this analysis, both the QC and PV layers have absorption step functions at their respective band gaps. The EQE of the PV layer is 100%. The overall quantum efficiency, η, of the quantum cutter varies from 100 to 200%, and its band gap is defined as twice the band gap of the PV layer. (B) Slices at different QC efficiencies, illustrating that the ideal PV band gap shifts as the QC layer's efficiency changes. Black dots reveal the maximum PCE for each trace, and the dashed line shows silicon's band gap. (C) The ideal QC band gap for different overall QC efficiencies, assuming a PV band gap of half this value. A presentation of the same data in nm is provided in the ESI.†

Consequently, when the perovskite band gap shifts below twice the Yb^{3+} $^2F_{5/2} \rightarrow {}^2F_{7/2}$ transition energy ($x > 0.84$), quantum cutting is no longer thermodynamically feasible and the PLQY decreases to $<10\%$.[21,23] This QC energy threshold is indicated by the shaded region in Fig. 3A.

Because the Yb^{3+} PL is not tunable, an optimized QC/PV device based on Yb^{3+}:$CsPb(Cl_{1-x}Br_x)_3$ as the QC layer must involve a PV layer whose response is well matched to this PL energy. Fig. 3B shows EQE curves for several state-of-the-art PV

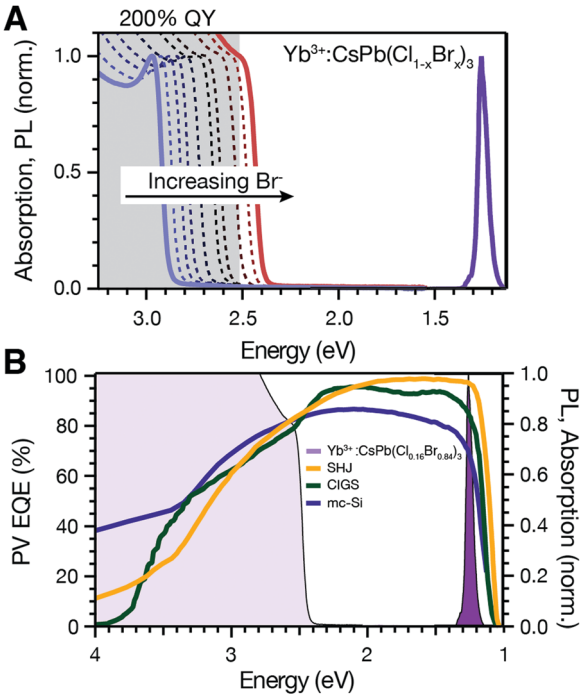

Fig. 3 (A) Representative experimental absorption and photoluminescence spectra of a high-efficiency Yb^{3+}:$CsPb(Cl_{1-x}Br_x)_3$ quantum-cutting material. The grey region illustrates the quantum-cutting regime. Below x = 0.84, the PLQY is 200%; above x = 0.84, the PLQY is < 10%. (B) The EQE characteristics of Si heterojunction, CIGS, and multicrystalline-Si and the absorption and near-infrared (~1.26 eV) emission of Yb^{3+}:$CsPb(Cl_{0.16}Br_{0.84})_3$. These absorption, photoluminescence, and EQE data are used in Fig. 4.

devices.[14,37] Unlike the Shockley–Queisser PV layer analyzed in Fig. 2, Si heterojunction[38] (SHJ), CIGS,[39,40] and multicrystalline-Si[41] (mc-Si) all exhibit poor EQEs from blue and UV photons because of nonradiative recombination[42,43] linked to surface defects or parasitic absorption.[44] This deficiency of real-world PV devices makes addition of a QC layer even more attractive, as it lowers the QC performance required to improve overall QC/PV device efficiency. Among these three PV devices, SHJ shows the highest EQE at the Yb^{3+} emission energy and would therefore be best suited for use in a QC/PV device when paired with Yb^{3+}:$CsPb(Cl_{1-x}Br_x)_3$.

Fig. 4A–C shows the absolute increases in PCE predicted for QC/PV devices formed by layering Yb^{3+}:$CsPb(Cl_{1-x}Br_x)_3$ onto SHJ, CIGS, and mc-Si PVs, plotted as a function of halide composition and η. For all PV layers, the maximum device efficiency occurs when the QC layer absorbs the largest number of photons and operates at the highest η—that is, at x = 0.84 with an η of 200%. Application of the perovskite QC material at these conditions yields a maximum PCE increase of 5.3%, 4.2%, and 3.5% for SHJ, CIGS, and mc-Si, respectively, corresponding to increases of 21%, 18%, and 13% relative to the PV PCEs alone. Although these PCE gains stem in part from the poor blue and UV responses of all three PVs, they are also extremely sensitive to the EQE at the energy of Yb^{3+} photoluminescence. EQEs of 98%, 85%, and 69% at ~1.26 eV have been recorded for SHJ, CIGS, and mc-Si, respectively.

Fig. 4A–C also demonstrates that, at low η, increasing x in the Yb^{3+}:$CsPb(Cl_{1-x}Br_x)_3$ QC layer decreases the QC/PV PCE. This decrease results when the QC layer absorbs in regions of high PV EQE, when the photoluminescence from the QC layer is inefficiently optically coupled into the PV device, or when saturation effects decrease the QC layer's PLQY as discussed below. As highlighted by Fig. 2C, these results imply that the optimal QC band-gap energy depends on a convolution of the solar spectrum, the η, and the EQE of the PV layer. Fig. 4D plots the optimal QC band-gap energy as a function of η for the same three PV layers using their experimental EQEs from Fig. 3B. For example, the optimal QC band gap for SHJ PV devices ranges from 2.40 eV (at η = 200%) to 2.81 eV (at η = 100%). These results for real-world PVs contrast with those in Fig. 2C calculated for an idealized PV, where the optimized QC band-gap varied from 1.90 to 2.67 eV depending on η.

The above analysis shows that Yb^{3+}:$CsPb(Cl_{1-x}Br_x)_3$ quantum cutters are particularly well suited for pairing with SHJ PV to improve overall PCEs. In fact, this QC/PV pair is remarkably close to the ideal pairing predicted strictly from thermodynamic considerations. To illustrate, Fig. 5A shows the PCE of a QC/PV pair integrating a SHJ PV with an ideal QC layer of varying band gap, plotted *vs.* the energy gap of the QC layer. The symbol in Fig. 5A represents Yb^{3+}:$CsPb(Cl_{0.16}Br_{0.84})_3$, and falls very close to the predicted maximum. Fig. 5B compares the absorption and photoluminescence spectra of the idealized QC layer with the experimental spectra of band-gap-optimized Yb^{3+}:$CsPb(Cl_{1-x}Br_x)_3$ QCs. Also included in this plot is the SHJ EQE. The band-gap (2.53 eV) and photoluminescence (1.26 eV) energies of Yb^{3+}:$CsPb(Cl_{0.16}Br_{0.84})_3$ are remarkably close to the band-gap (2.40 eV) and photoluminescence (1.20 eV) energies of the best possible quantum cutter for pairing with SHJ. These comparisons underscore the exceptional potential of Yb^{3+}:$CsPb(Cl_{1-x}Br_x)_3$ quantum cutters to enhance the PCE of SHJ solar cells. Fig. 5C illustrates the spectral irradiance utilization in the Yb^{3+}:$CsPb(Cl_{0.16}Br_{0.84})_3$/SHJ QC/PV device. Comparing the dark blue area to the green area at the same energies highlights the significant reduction in thermalization losses that can be achieved through this pairing.

At high photoexcitation rates the Yb^{3+} PL from Yb^{3+}:$CsPb(Cl_{1-x}Br_x)_3$ saturates and the PLQY decreases.[21,23] This saturation results from an efficient nonradiative Auger cross-relaxation process that outcompetes quantum cutting when photoexcitation rates exceed the Yb^{3+} $^2F_{5/2}$ relaxation rate. As discussed in ref. 27, this saturation may have serious implications for the utility of these materials in solar downconversion schemes, but several promising routes to remedy this issue have been identified. To understand the effect of saturation on the model results presented above, we expanded our simulations to account for the flux-dependent PLQY of Yb^{3+}:$CsPb(Cl_{1-x}Br_x)_3$. Fig. 6A shows the hourly photon flux (4.13 to 2.53 eV, or 300 to 490 nm) absorbed by an optimized Yb^{3+}:$CsPb(Cl_{1-x}Br_x)_3$ (x = 0.84) quantum cutter for a typical meteorological year (TMY) in Seattle, WA (USA).[45] The photon flux increases during the middle of the day as the atmospheric pathlength decreases. Similarly, the photon flux decreases during the winter months due to the reduced hours

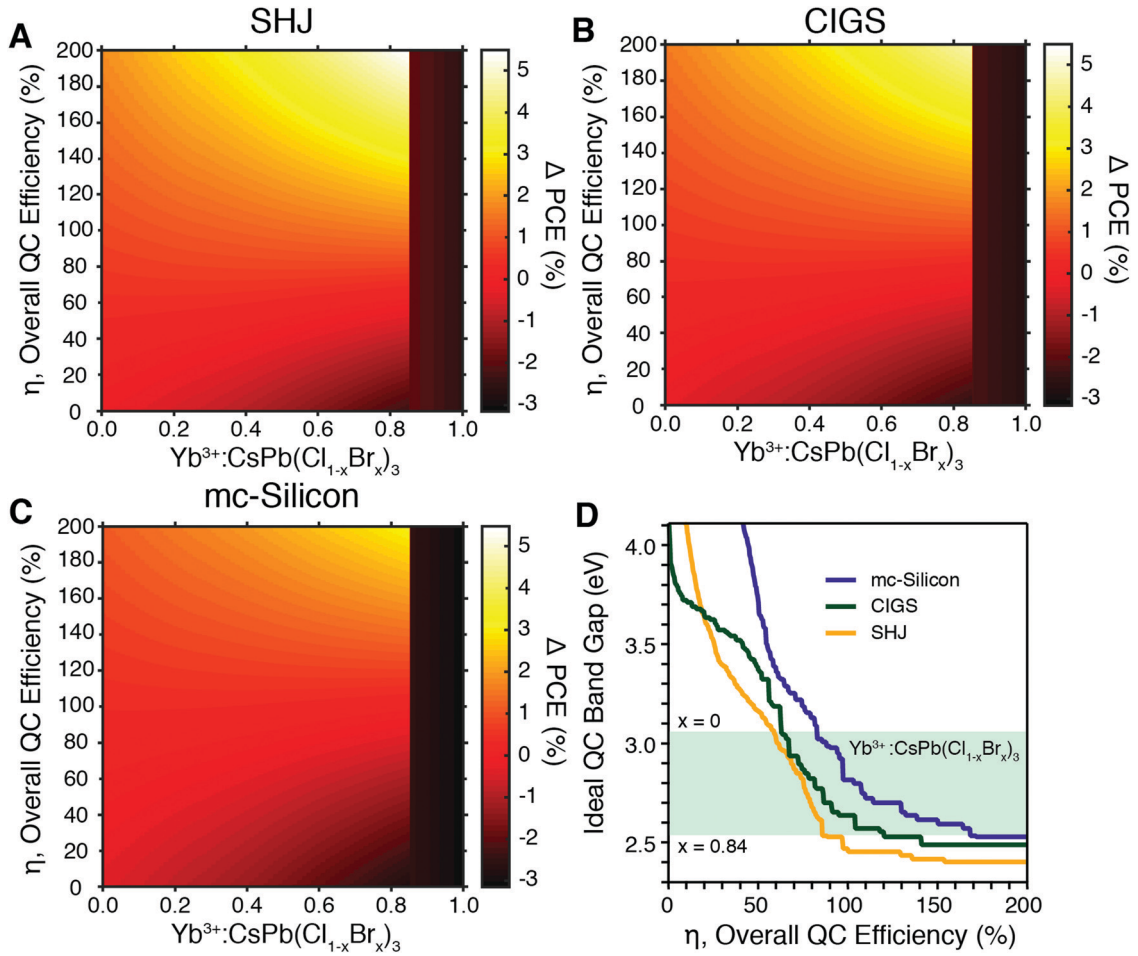

Fig. 4 The detailed-balance maximum PCE increase by adding Yb^{3+}:$CsPb(Cl_{1-x}Br_x)_3$ onto (A) SHJ, (B) CIGS, and (C) mc-Si at different overall quantum-cutting efficiencies. The Yb^{3+}:$CsPb(Cl_{1-x}Br_x)_3$ absorption spectrum varies with halide composition. From x = 0.84 to 1.00, the $CsPb(Cl_{1-x}Br_x)_3$ host lattice's band gap is insufficient to produce two excited Yb^{3+} ions, and its PLQY drops to <10%. (D) The ideal quantum-cutting band gap for different PV layers described in Fig. 3. For this analysis, a non-ideal QC layer is used where the PL energy is fixed at one half of the QC band gap. The green box indicates synthetically accessible Yb^{3+}:$CsPb(Cl_{1-x}Br_x)_3$ compositions that can thermodynamically undergo QC.

of daylight at Seattle's latitude of 49.49°. The maximum hourly absorbed photon flux is 3.5×10^{20} photons m^{-2}. For comparison, the PLQY drops from 200 to 100% at an overall absorbed flux of $\sim 7 \times 10^{20}$ photons m^{-2}.[27]

Fig. 6B shows the corresponding hourly PLQY of the QC layer, which correlates inversely to the absorbed photon flux in Fig. 6A. From Fig. 6B, the PLQY reaches its maximum value at the beginning and end of each day due to the low photon fluxes at these times. Similarly, it reaches and stays near its maximum for most daylight hours throughout winter. During summer, the PLQY decreases to an annual minimum of 126%, illustrating that although saturation does decrease the performance of the QC process, the QC layer should still always improve the SHJ device performance, provided the optical coupling is sufficiently large. Because QC PLQYs only affect performance under illumination, we calculated the hourly power produced by an integrated QC/PV device, including the flux-dependent PLQY. Fig. 6C shows these QC/PV hourly energy yields, calculated assuming 100% optical coupling of the QC PL. The device performance varies with the overall incident spectral power, reaching a maximum around noon each day and decreasing from summer to winter.

Tying these calculations together, Fig. 6D summarizes the relative gain in energy yield afforded by applying an Yb^{3+}:$CsPb(Cl_{0.16}Br_{0.84})_3$ QC layer to SHJ PV. These results show that the benefits of the QC layer track its PLQY. At every hour of illumination in the Seattle TMY, PL saturation is not too severe to negate the benefits of the QC layer, and consequently the QC layer increases the hourly energy yield of the underlying PV. The time-averaged gain in annual power generation is 15.0% (relative). The power-generation gains are maximized in winter and at the beginnings and ends of each day, when saturation is minimized, and they're reduced in summer and in the middles of the days, when saturation becomes relevant. For example, the maximum (18%) increase in energy yield occurs on April 24th at 10 a.m. in this data set, and the minimum (9.7%) occurs on June 26th at 2 p.m. Importantly, both limits correspond to a net gain.

Summing each hour of the energy yield generates the annual energy yield of the QC/PV device. Fig. 7 compares the annual energy yield for a QC/SHJ device operating in Seattle, WA and

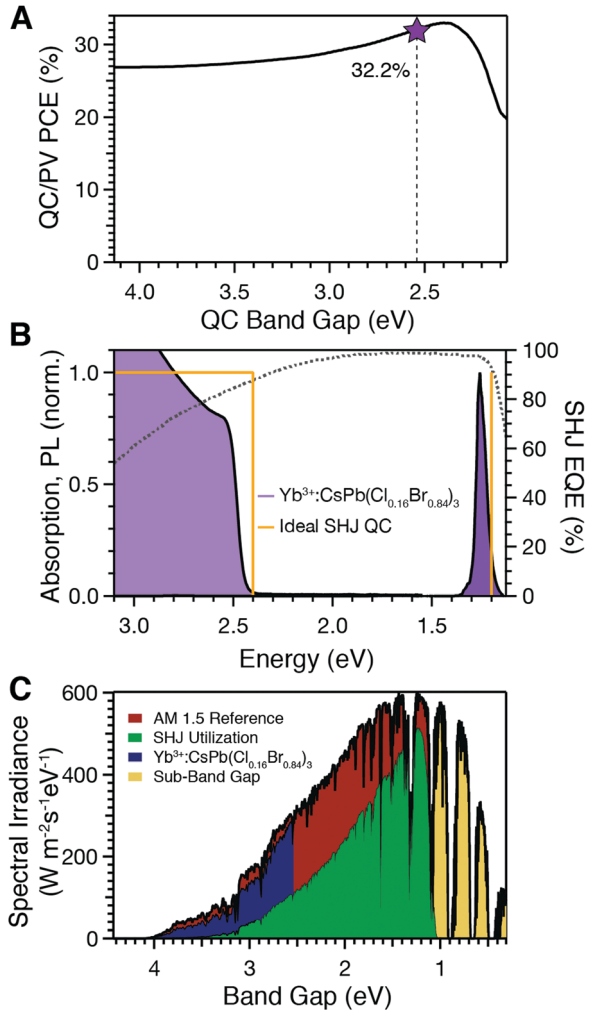

Fig. 5 Comprehensive analysis of a Yb^{3+}:$CsPb(Cl_{1-x}Br_x)_3$/SHJ QC/PV device. (A) Detailed balance PCE of an SHJ PV paired with a perfect QC material. The star indicates the bandgap-optimized Yb^{3+}:$CsPb(Cl_{1-x}Br_x)_3$ quantum cutter, illustrating a PCE of 32.2%. (B) Absorption and photoluminescence spectra of the ideal QC layer and a real-world optimized Yb^{3+}:$CsPb(Cl_{0.16}Br_{0.84})_3$ QC layer. The dashed curve plots the EQE of SHJ PV. (C) Use of spectral irradiance in the optimized Yb^{3+}:$CsPb(Cl_{0.16}Br_{0.84})_3$ on SHJ QC/PV device. The predicted EQEs of the SHJ QC/PV device are provided in the ESI.†

Golden, CO (USA) with and without 2-axis tracking, calculated for 50, 75, and 100% optical coupling efficiencies (ξ in eqn (4) and (6)) using experimental saturation characteristics and, for reference, also at 100% optical coupling efficiency in the limit of no PLQY saturation. Golden was selected to illustrate the flux-dependence of the quantum cutter because of the high direct normal irradiance (DNI) at this location. 50% optical coupling efficiency was chosen to illustrate the scenario in which half of the QC-emitted photons are lost, corresponding to the worst-case scenario of isotropic emission without QC-to-PV photonic coupling. Notably, in all scenarios, the QC layer improves the device performance. These results illustrate that even the worst-case scenario of isotropic QC-photon emission combined with the experimental flux-dependent PLQY will not prevent improvement of SHJ PV performance by Yb^{3+}:$CsPb(Cl_{1-x}Br_x)_3$ QC layers in a wide range of geographic locations, and they highlight the potential rewards that could be obtained by reducing PL saturation and increasing optical coupling efficiencies. For example, optical coupling efficiencies of up to 88% have been predicted for II–VI nanocrystals[46,47] and luminescent glasses[48] on mc-Si by tuning refractive indices to optimize internal reflection. Strikingly, the annual energy yields obtainable from these Yb^{3+}:$CsPb(Cl_{1-x}Br_x)_3$/SHJ QC/PV devices compare favorably with those obtainable from perovskite-on-silicon tandem devices, but are achieved without the need for additional electrical contacts, recombination layers, inverters, or current matching.[4]

Conclusion

The results presented here assess the potential efficiency gains that can be obtained by interfacing quantum-cutting Yb^{3+}:$CsPb(Cl_{1-x}Br_x)_3$ downconversion films with single-junction PV. Our detailed-balance calculations demonstrate that Yb^{3+}:$CsPb(Cl_{1-x}Br_x)_3$ is a powerful quantum cutter that can substantially improve the performance of a wide range of PV technologies, despite its PL saturation and without optimizing optical coupling between QC and PV layers. In all cases, increased PCEs are achieved by reducing thermalization, reflection, and nonradiative-recombination losses from blue and UV photons, with specific improvements reflecting the particular PV's UV/blue and near-IR EQE values and the specific QC characteristics (energy gap, PLQY, *etc.*). The ability to tune the band gap of Yb^{3+}:$CsPb(Cl_{1-x}Br_x)_3$ by varying the halide composition enables QC layers to be tailored for optimization with specific PV partners. Among the QC/PV pairs considered here, we find that Yb^{3+}:$CsPb(Cl_{0.16}Br_{0.84})_3$ has bandgap and PL energies that are especially well-matched for pairing with SHJ PVs. For all PV technologies investigated, Yb^{3+}:$CsPb(Cl_{0.16}Br_{0.84})_3$ QCs are predicted to yield significant performance gains even without additional engineering to enhance optical coupling. Yb^{3+}:$CsPb(Cl_{1-x}Br_x)_3$ is thus not only an exceptional QC material in its own right, but our results also demonstrate that many of its specific properties are also almost exactly optimized for QC/PV applications.

A particular concern prior to this work was whether the PL saturation of Yb^{3+}:$CsPb(Cl_{1-x}Br_x)_3$ might completely offset any potential efficiency gains under real-world solar illumination. Although PL saturation is facile in these materials, we find that real-world incident solar photon fluxes are in fact insufficient to negate the benefits of the QC layer. In part, this result reflects the fact that the incident solar photon flux is more often less than AM1.5G (where PL saturation is less important) than it is greater than AM1.5G. Our calculations combining PL saturation and real-world photon fluxes demonstrate that Yb^{3+}:$CsPb(Cl_{1-x}Br_x)_3$ boosts performance in widely different geographic locations with substantially different spectral irradiances. Further gains can still be achieved by suppressing saturation, and Erickson *et al.* have outlined several potential routes to reduce PL saturation in Yb^{3+}:$CsPb(Cl_{1-x}Br_x)_3$.[27]

These calculations also highlight another key insight, namely that there is significant interplay between the QC PLQY, QC/PV

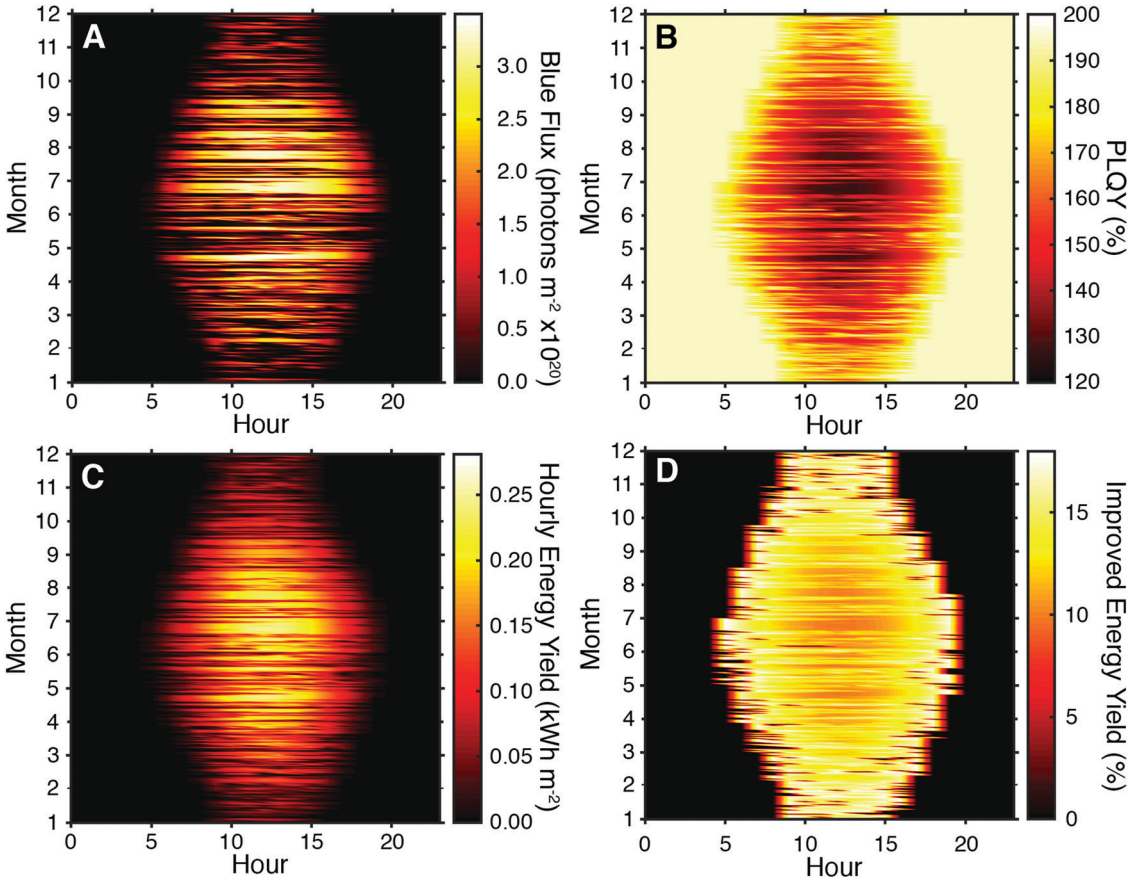

Fig. 6 The impact of flux-dependent quantum yields for a Yb^{3+}:$CsPb(Cl_{0.16}Br_{0.84})_3$/SHJ QC/PV device, represented for a typical meteorological year in Seattle, WA, USA. (A) The average hourly, global horizontal irradiance (GHI, non-concentrated) photon flux from 300 to 490 nm absorbed by an optimized Yb^{3+}:$CsPb(Cl_{1-x}Br_x)_3$ quantum cutter, plotted for each hour of each day over the course of a year. (B) The hourly PLQY of the QC material using the data from panel (A) and experimental PL saturation results from ref. 27. (C) The areal hourly energy yield of the QC/PV device, calculated using the model from Fig. 4 and assuming 100% optical coupling of the QC PL (ξ in eqn (4) and (6)). (D) The corresponding percent increase in areal hourly energy yield relative to a standard SHJ PV without a QC layer, in Seattle. Fig. S3 in the ESI† shows the total monthly blue photon flux and the average PLQY, as well as the daily energy yield and improved energy yield.

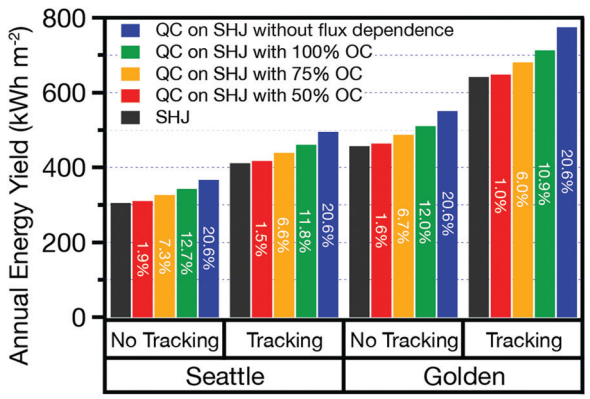

Fig. 7 The areal annual energy production yield of a Yb^{3+}:$CsPb(Cl_{1-x}Br_x)_3$/SHJ QC/PV device with and without 2-axis tracking mechanisms and for different efficiencies of optical coupling (ξ in eqn (4) and (6)), including the effects of flux-dependent PLQY. Relative percentage increases are labeled on each bar. Results are presented for two geographic locations in the United States, Seattle, WA and Golden, CO.

optical coupling, and optimized QC and PV energy gaps. Because of this interplay, the energy gaps of QC and PV materials that will generate an optimized QC/PV device vary by several hundred meV, from 1.9 to 2.7 eV, depending on the actual QC PLQY and QC/PV optical-coupling efficiency. In comparison, previous fully idealized detailed-balance calculations predicted a single optimal QC band gap of 2.2 eV for pairing with Si PV.[3] While valuable, idealized detailed-balance calculations do not sufficiently guide real-world device implementation because of this interplay. In addition to assessing maximum efficiency gains, the results presented here thus also provide practical design rules for constructing high-efficiency QC/PV devices based on real-world materials and conditions that will help to accelerate the development of high-performance solar technologies.

For optical management, introducing Bragg mirrors,[49] adding anti-reflective coatings,[28] or engineering non-radiative energy-transfer processes can be expected to enhance optical coupling between QC and PV layers,[50] but were not included in this analysis. In addition to improvements in PCE through spectral shaping, QC layers or photonic structures added for enhanced optical coupling may also benefit the PV in other ways that are also not included in these calculations, such as limiting radiative recombination losses[51] or enhancing transmission of light *via*

refractive-index grading.[28,52] For example, QC layers can reduce the heat load of a PV device by reducing thermalization. PV performance is highly sensitive to temperature, and typical PV PCEs decrease by $\sim$0.5 absolute % K^{-1} above ambient conditions.[53] Given the wide range of operating conditions of PV devices, which reach 75 °C in some cases, this precipitous decline in performance at high temperatures threatens to seriously reduce PV performance.[54–56] Because this reduction is exacerbated during peak power generation due to solar heat load, active cooling methods, such as water cooling, are often introduced to limit PV temperatures.[54,55] In comparison, real world heat loads on PV devices are approximately 300 to 400 W.[56] The application of a front-face Yb^{3+}:$CsPb(Cl_{1-x}Br_x)_3$ QC layer reduces the heat load by $\sim$100 W for SHJ, CIGS, and mc-Si technologies under one-sun, AM1.5G illumination. Thus, the reduced heating afforded by the QC material promises to markedly improve PV device performance. These potential gains are not included in this analysis.

Also omitted from this analysis is the possibility of tailoring the PV to suit the spectral characteristics of the Yb^{3+}:$CsPb(Cl_{1-x}Br_x)_3$ QC layer, in particular the Yb^{3+} photoluminescence energy. For example, narrowing the CIGS energy gap in Fig. 3B would improve EQE at the Yb^{3+} photoluminescence substantially. The ability to tailor energy gaps in CIGS[39] and similarly tunable materials[40] through composition control makes these PV platforms especially attractive for QC/PV applications. Because of the absence of electrical connectivity in these QC/PV devices, the QC modification should be easily transferrable among PV technologies. Additionally, compared to their hybrid organic–inorganic perovskite counterparts, whose PV applications are hindered by water- or oxygen-induced degradation[57,58] and photoinduced anion segregation,[59,60] these all-inorganic $CsPb(Cl_{1-x}Br_x)_3$ perovskites are relatively moisture stable,[61] and Yb^{3+} doping eliminates photoinduced anion segregation.[21] Moreover, experimental methods developed[62] for suppressing ion migration, lead leaching, and moisture sensitivity in hybrid perovskites should translate readily to these Yb^{3+}:$CsPb(Cl_{1-x}Br_x)_3$ materials.

In summary, the results presented here indicate that simple optical integration of Yb^{3+}:$CsPb(Cl_{1-x}Br_x)_3$ QC layers with high-efficiency PV devices can yield marked performance gains, and that there is even further room for improvement with additional device engineering. The present results illustrate that pairing SHJ PV with Yb^{3+}:$CsPb(Cl_{1-x}Br_x)_3$ QC layers improves device performance despite PL saturation and non-unity optical coupling. By the same token, these results also highlight the potential benefits still to be gained by reducing PL saturation and increasing optical coupling, and advances in these two directions appear promising.

Conflicts of interest

There are no conflicts of interest to declare.

Acknowledgements

This research was supported by the National Science Foundation (NSF) through the UW Molecular Engineering Materials Center, a Materials Research Science and Engineering Center (DMR-1719797). Additional support from DMR-1807394 (to DRG) and the Washington Research Foundation (to MJC and DMK) is gratefully acknowledged.

References

1 B. M. van der Ende, L. Aarts and A. Meijerink, *Phys. Chem. Chem. Phys.*, 2009, **11**, 11081–11095.
2 J. Nelson, *The Physics of Solar Cells*, Imperial College Press, London, 2003.
3 T. Trupke, M. A. Green and P. Würfel, *J. Appl. Phys.*, 2002, **92**, 1668–1674.
4 M. T. Hörantner and H. J. Snaith, *Energy Environ. Sci.*, 2017, **10**, 1983–1993.
5 M. T. Hörantner, T. Leijtens, M. E. Ziffer, G. E. Eperon, M. G. Christoforo, M. D. McGehee and H. J. Snaith, *ACS Energy Lett.*, 2017, **2**, 2506–2513.
6 G. E. Eperon, T. Leijtens, K. A. Bush, R. Prasanna, T. Green, J. T.-W. Wang, D. P. McMeekin, G. Volonakis, R. L. Milot, R. May, A. Palmstrom, D. J. Slotcavage, R. A. Belisle, J. B. Patel, E. S. Parrott, R. J. Sutton, W. Ma, F. Moghadam, B. Conings, A. Babayigit, H.-G. Boyen, S. Bent, F. Giustino, L. M. Herz, M. B. Johnston, M. D. McGehee and H. J. Snaith, *Science*, 2016, **354**, 861–865.
7 B. Chen, Z. Yu, K. Liu, X. Zheng, Y. Liu, J. Shi, D. Spronk, P. N. Rudd, Z. Holman and J. Huang, *Joule*, 2019, **3**, 177–190.
8 A. D. Vos, *J. Phys. D: Appl. Phys.*, 1980, **13**, 839–846.
9 F. Sahli, J. Werner, B. A. Kamino, M. Bräuninger, R. Monnard, B. Paviet-Salomon, L. Barraud, L. Ding, J. J. D. Leon, D. Sacchetto, G. Cattaneo, M. Despeisse, M. Boccard, S. Nicolay, Q. Jeangros, B. Niesen and C. Ballif, *Nat. Mater.*, 2018, **17**, 820.
10 I. L. Braly, D. W. deQuilettes, L. M. Pazos-Outón, S. Burke, M. E. Ziffer, D. S. Ginger and H. W. Hillhouse, *Nat. Photonics*, 2018, **12**, 355.
11 G. E. Eperon, M. T. Hörantner and H. J. Snaith, *Nat. Rev. Chem.*, 2017, **1**, 0095.
12 M. Jaysankar, M. Filipič, B. Zielinski, R. Schmager, W. Song, W. Qiu, U. W. Paetzold, T. Aernouts, M. Debucquoy, R. Gehlhaar and J. Poortmans, *Energy Environ. Sci.*, 2018, **11**, 1489–1498.
13 Y. (Michael) Yang, Q. Chen, Y.-T. Hsieh, T.-B. Song, N. D. Marco, H. Zhou and Y. Yang, *ACS Nano*, 2015, **9**, 7714–7721.
14 B. Chen, Y. Bai, Z. Yu, T. Li, X. Zheng, Q. Dong, L. Shen, M. Boccard, A. Gruverman, Z. Holman and J. Huang, *Adv. Energy Mater.*, 2016, **6**, 1601128.
15 W. Shockley and H. J. Queisser, *J. Appl. Phys.*, 1961, **32**, 510–519.
16 B. M. van der Ende, L. Aarts and A. Meijerink, *Adv. Mater.*, 2009, **21**, 3073–3077.
17 D.-C. Yu, R. Martín-Rodríguez, Q.-Y. Zhang, A. Meijerink and F. T. Rabouw, *Light: Sci. Appl.*, 2015, **4**, e344.
18 P. Vergeer, T. J. H. Vlugt, M. H. F. Kox, M. I. den Hertog, J. P. J. M. van der Eerden and A. Meijerink, *Phys. Rev. B: Condens. Matter Mater. Phys.*, 2005, **71**, 014119.

19 Y. Teng, J. Zhou, X. Liu, S. Ye and J. Qiu, *Opt. Express*, 2010, **18**, 9671–9676.
20 T. J. Milstein, D. M. Kroupa and D. R. Gamelin, *Nano Lett.*, 2018, **18**, 3792–3799.
21 D. M. Kroupa, J. Y. Roh, T. J. Milstein, S. E. Creutz and D. R. Gamelin, *ACS Energy Lett.*, 2018, **3**, 2390–2395.
22 G. Pan, X. Bai, D. Yang, X. Chen, P. Jing, S. Qu, L. Zhang, D. Zhou, J. Zhu, W. Xu, B. Dong and H. Song, *Nano Lett.*, 2017, **17**, 8005–8011.
23 T. J. Milstein, K. T. Kluherz, D. M. Kroupa, C. S. Erickson, J. J. De Yoreo and D. R. Gamelin, *Nano Lett.*, 2019, **19**, 1931–1937.
24 D. Zhou, D. Liu, G. Pan, X. Chen, D. Li, W. Xu, X. Bai and H. Song, *Adv. Mater.*, 2017, **29**, 1704149.
25 M. J. Crane, D. Kroupa, J. Y. D. Roh, R. T. Anderson, M. D. Smith and D. R. Gamelin, *ACS Appl. Energy Mater.*, DOI: 10.1021/acsaem.9b00910.
26 T. A. Cohen, T. J. Milstein, D. M. Kroupa, J. D. MacKenzie, C. K. Luscombe and D. R. Gamelin, *J. Mater. Chem. A*, 2019, **7**, 9279–9288.
27 C. S. Erickson, M. J. Crane, T. J. Milstein and D. R. Gamelin, *J. Phys. Chem. C*, 2019, **19**, 12474–12484.
28 A. De Vos, A. Szymanska and V. Badescu, *Energy Convers. Manage.*, 2009, **50**, 328–336.
29 T. Markvart, *J. Appl. Phys.*, 2006, **99**, 026101.
30 V. Badescu, A. D. Vos, A. M. Badescu and A. Szymanska, *J. Phys. D: Appl. Phys.*, 2007, **40**, 341–352.
31 V. Badescu and A. De Vos, *J. Appl. Phys.*, 2007, **102**, 073102.
32 Z. R. Abrams, A. Niv and X. Zhang, *J. Appl. Phys.*, 2011, **109**, 114905.
33 O. M. ten Kate, M. de Jong, H. T. Hintzen and E. van der Kolk, *J. Appl. Phys.*, 2013, **114**, 084502.
34 D. L. Dexter, *Phys. Rev.*, 1957, **108**, 630–633.
35 S. Rühle, *Sol. Energy*, 2016, **130**, 139–147.
36 C. Strümpel, M. McCann, G. Beaucarne, V. Arkhipov, A. Slaoui, V. Švrček, C. del Cañizo and I. Tobias, *Sol. Energy Mater. Sol. Cells*, 2007, **91**, 238–249.
37 M. Powalla, S. Paetel, D. Hariskos, R. Wuerz, F. Kessler, P. Lechner, W. Wischmann and T. M. Friedlmeier, *Engineering*, 2017, **3**, 445–451.
38 Z. C. Holman, M. Filipič, A. Descoeudres, S. De Wolf, F. Smole, M. Topič and C. Ballif, *J. Appl. Phys.*, 2013, **113**, 013107.
39 J. Ramanujam and U. P. Singh, *Energy Environ. Sci.*, 2017, **10**, 1306–1319.
40 A. R. Uhl, J. K. Katahara and H. W. Hillhouse, *Energy Environ. Sci.*, 2016, **9**, 130–134.
41 C. Battaglia, A. Cuevas and S. D. Wolf, *Energy Environ. Sci.*, 2016, **9**, 1552–1576.
42 K. Masuko, M. Shigematsu, T. Hashiguchi, D. Fujishima, M. Kai, N. Yoshimura, T. Yamaguchi, Y. Ichihashi, T. Mishima, N. Matsubara, T. Yamanishi, T. Takahama, M. Taguchi, E. Maruyama and S. Okamoto, *IEEE J. Photovolt.*, 2014, **4**, 1433–1435.
43 J. A. Giesecke, M. Kasemann, M. C. Schubert, P. Würfel and W. Warta, *Prog. Photovoltaics Res. Appl.*, 2010, **18**, 10–19.
44 H. Savin, P. Repo, G. von Gastrow, P. Ortega, E. Calle, M. Garín and R. Alcubilla, *Nat. Nanotechnol.*, 2015, **10**, 624–628.
45 M. Sengupta, Y. Xie, A. Lopez, A. Habte, G. Maclaurin and J. Shelby, *Renewable Sustainable Energy Rev.*, 2018, **89**, 51–60.
46 S. Kalytchuk, S. Gupta, O. Zhovtiuk, A. Vaneski, S. V. Kershaw, H. Fu, Z. Fan, E. C. H. Kwok, C.-F. Wang, W. Y. Teoh and A. L. Rogach, *J. Phys. Chem. C*, 2014, **118**, 16393–16400.
47 C.-Y. Huang, D.-Y. Wang, C.-H. Wang, Y.-T. Chen, Y.-T. Wang, Y.-T. Jiang, Y.-J. Yang, C.-C. Chen and Y.-F. Chen, *ACS Nano*, 2010, **4**, 5849–5854.
48 F. Steudel, S. Loos, B. Ahrens and S. Schweizer, *J. Lumin.*, 2015, **164**, 76–80.
49 N. D. Bronstein, Y. Yao, L. Xu, E. O'Brien, A. S. Powers, V. E. Ferry, A. P. Alivisatos and R. G. Nuzzo, *ACS Photonics*, 2015, **2**, 1576–1583.
50 H. M. Nguyen, O. Seitz, W. Peng, Y. N. Gartstein, Y. J. Chabal and A. V. Malko, *ACS Nano*, 2012, **6**, 5574–5582.
51 E. D. Kosten, J. H. Atwater, J. Parsons, A. Polman and H. A. Atwater, *Light: Sci. Appl.*, 2013, **2**, e45.
52 M. Shravanth Vasisht, J. Srinivasan and S. K. Ramasesha, *Sol. Energy*, 2016, **131**, 39–46.
53 E. M. G. Rodrigues, R. Melício, V. M. F. Mendes and J. P. S. Catalão, *Renewable Energies and Power Quality Journal*, 2011, **1**, 369–373.
54 K. A. Moharram, M. S. Abd-Elhady, H. A. Kandil and H. El-Sherif, *Ain Shams Eng. J.*, 2013, **4**, 869–877.
55 S. Nižetić, D. Čoko, A. Yadav and F. Grubišić-Čabo, *Energy Convers. Manage.*, 2016, **108**, 287–296.
56 İ. Ceylan, A. E. Gürel, H. Demircan and B. Aksu, *Energy Build.*, 2014, **72**, 96–101.
57 Q. Wang, B. Chen, Y. Liu, Y. Deng, Y. Bai, Q. Dong and J. Huang, *Energy Environ. Sci.*, 2017, **10**, 516–522.
58 X. Zhang, X. Ren, B. Liu, R. Munir, X. Zhu, D. Yang, J. Li, Y. Liu, D.-M. Smilgies, R. Li, Z. Yang, T. Niu, X. Wang, A. Amassian, K. Zhao and S. (Frank) Liu, *Energy Environ. Sci.*, 2017, **10**, 2095–2102.
59 E. T. Hoke, D. J. Slotcavage, E. R. Dohner, A. R. Bowring, H. I. Karunadasa and M. D. McGehee, *Chem. Sci.*, 2014, **6**, 613–617.
60 R. Giridharagopal, J. T. Precht, S. Jariwala, L. Collins, S. Jesse, S. V. Kalinin and D. S. Ginger, *ACS Nano*, 2019, **13**, 2812–2821.
61 H. Huang, M. I. Bodnarchuk, S. V. Kershaw, M. V. Kovalenko and A. L. Rogach, *ACS Energy Lett.*, 2017, **2**, 2071–2083.
62 R. Cheacharoen, N. Rolston, D. Harwood, K. A. Bush, R. H. Dauskardt and M. D. McGehee, *Energy Environ. Sci.*, 2018, **11**, 144–150.

